

Direct Observation of Alternating Octahedral and Prismatic Sodium Layers in O3-Type Transition Metal Oxides

Jae Chul Kim, Deok-Hwang Kwon, Julia H. Yang, Hyun-chul Kim, Shou-Hang Bo, Lijun Wu, Haegyeom Kim, Dong-Hwa Seo, Tan Shi, Jingyang Wang, Yimei Zhu, and Gerbrand Ceder*

The oxygen stacking of O3-type layered sodium transition metal oxides (O3-NaTMO₂) changes dynamically upon topotactic Na extraction and reinsertion. While the phase transition from octahedral to prismatic Na coordination that occurs at intermediate desodiation by transition metal slab gliding is well understood, the structural evolution at high desodiation, crucial to achieve high reversible capacity, remains mostly uncharted. In this work, the phase transitions of O3-type layered NaTMO₂ at high voltage are investigated by combining experimental and computational approaches. An OP2-type phase that consists of alternating octahedral and prismatic Na layers is directly observed by in situ X-ray diffraction and high-resolution scanning transmission electron microscopy. The origin of this peculiar phase is explained by atomic interactions involving Jahn–Teller active Fe⁴⁺ and distortion tolerant Ti⁴⁺ that stabilize the local Na environment. The path-dependent desodiation and resodiation pathways are also rationalized in this material through the different kinetics of the prismatic and octahedral layers, presenting a comprehensive picture about the structural stability of the layered materials upon Na intercalation.

1. Introduction

Layered Na transition metal oxides with stoichiometry NaTMO₂ (TM: transition metal combination) show promising properties as high-performance cathode materials for low-cost Na-ion batteries.^[1,2] In the discharged state, these materials are often isostructural with their lithium analogues: octahedrally coordinated Na or Li ions sit between layers of edge-sharing TMO₆ octahedra with a repeated stacking unit of three (e.g., the O3 structure).^[3] When charged, however, very different coordination preferences for Na⁺ and Li⁺ make their layered TM-oxides behave radically different.^[4] As the preferred coordinations of Li (octahedral and tetrahedral) can both be achieved in the ABCABC anion rocksalt packing of the O3 structure, oxygen stacking changes upon delithiation of LiTMO₂ compounds are rare.^[4] Rather,

they tend to suffer from TM-ion migration driven by the tendency of Li to occupy tetrahedral sites.^[5,6] In contrast, the octahedral and prismatic coordinations, which are preferred for Na, cannot be achieved in the same oxygen framework and require the gliding of oxygen layers to transform into each other. This gliding leads to a much more complex set of phase transformations for NaTMO₂ than that for the Li compounds.^[7–10] While most of these transformations appear reversible upon Na extraction and insertion, the hysteresis, inhomogeneity, and stresses associated with the more complex phase transitions in layered Na cathodes can lead to long term stability issues. Understanding these phases is particularly important as Na cathodes need to be charged to a relatively higher level of alkali extraction than Li compounds to make them competitive in light of their lower cell voltage.

For large-scale energy storage applications, Na-ion batteries utilizing Fe as a redox center are a promising low-cost alternative for Li-ion, which mostly relies on Co and Ni.^[1,2] However, fully reversible use of Fe redox is difficult. Deintercalation of a large amount of Na can destabilize the layered structure, leading to irreversible changes especially in materials with large Fe content (e.g., NaFeO₂).^[11–13] The nature of the highly desodiated phase regarding how it forms and how it creates irreversibility is unclear. X-ray diffraction (XRD) has indicated the presence of stacking faults,^[12] and pair-distribution function (PDF) analysis has been used to argue for TM migration.^[11]

Prof. J. C. Kim, Dr. D.-H. Kwon, J. H. Yang, Dr. H. Kim, Prof. S.-H. Bo, Dr. H. Kim, Dr. T. Shi, J. Wang, Prof. G. Ceder
Materials Sciences Division
Lawrence Berkeley National Laboratory
Berkeley, CA 94720, USA
E-mail: gceder@berkeley.edu


Prof. J. C. Kim
Department of Chemical Engineering and Materials Science
Stevens Institute of Technology
Hoboken, NJ 07030, USA

Dr. D.-H. Kwon, J. H. Yang, Prof. D.-H. Seo, Dr. T. Shi, J. Wang, Prof. G. Ceder
Department of Materials Science and Engineering
University of California Berkeley
Berkeley, CA 94720, USA

Prof. S.-H. Bo
University of Michigan-Shanghai Jiao Tong University Joint Institute
Shanghai Jiao Tong University
Shanghai 200240, China

Dr. L. Wu, Dr. Y. Zhu
Condensed Matter Physics and Materials Science Department
Brookhaven National Laboratory
Upton, NY 11973, USA

Prof. D.-H. Seo
Department of Energy Engineering
Ulsan National Institute of Science and Technology (UNIST)
Ulsan 44919, Republic of Korea

 The ORCID identification number(s) for the author(s) of this article can be found under <https://doi.org/10.1002/aenm.202001151>.

DOI: 10.1002/aenm.202001151

Yabuuchi et al. proposed a structural model for highly desodiated P2-type $\text{Na}_{0.67}\text{Fe}_{0.5}\text{Mn}_{0.5}\text{O}_2$.^[12] In their model, Na occupies a prismatic site in between two TMO_6 slabs with a repeating period of two (ABBA stacking in comparison to ABCABC in O3). They found that at 4.2 V the P2 stacking undergoes a phase transition into an unknown phase by comparing the simulated and observed XRD patterns. They suggested that the stacking of this unknown phase contains alternating octahedral and prismatic Na layers and named it “OP4” (ABBACBBC oxygen stacking).^[12,14] Very recently, Somerville et al. investigated the structural evolution of P2-type layered $\text{Na}_{2/3}\text{Ni}_{1/6}\text{Mn}_{1/2}\text{Fe}_{1/3}\text{O}_2$ (33% Fe in the TM layer), and observed that in the high-voltage phase, prismatic and octahedral Na coexist.^[15]

In this work, the unusual phase observed at the very high state of charge in layered Na compounds is investigated. We provide a comprehensive perspective on the phase transitions in $\text{O3-NaTi}_{0.25}\text{Fe}_{0.25}\text{Co}_{0.25}\text{Ni}_{0.25}\text{O}_2$, a compound that shows high energy density and good cycle life.^[16,17] By combining in situ XRD, high resolution-scanning transmission electron microscopy (HR-STEM), X-ray absorption spectroscopy (XAS), and first-principles modeling, we visualize and rationalize the structural change in this O3-type transition metal oxide at high voltage. Our finding is that the strong Jahn–Teller (JT) distortion effect in Fe^{4+} creates a Na–O– Fe^{4+} interaction which can be better accommodated in a structure in which octahedral and prismatic Na stackings alternate, stabilizing an OP2-type (ABCAABCA stacking) structure. This result provides insight into the origin of the alternating O–P Na layer formation. We also relate our findings to other work on layered Na oxides that contain a certain concentration of Jahn–Teller ions, where the intergrowth of different stackings is also observed.^[11–13,15] We propose a mechanism that may promote structural stability at high state of charge, potentially leading to better understanding of high voltage stability of Na-ion batteries.

2. Results

Neutron scattering was used to identify the stacking of the structure, lattice parameters, and site occupancies for the synthesized material. **Figure 1a** shows a neutron Bragg diffraction pattern obtained from as-prepared $\text{NaTi}_{0.25}\text{Fe}_{0.25}\text{Co}_{0.25}\text{Ni}_{0.25}\text{O}_2$ (NaTFCN). The structure fits well to the $R\bar{3}m$ symmetry with the ABCABC O3-stacking model. From Rietveld refinement results, we obtain $a = 2.9893(4)$ Å and $c = 16.0155(0)$ Å, in good agreement with the literature.^[16] The occupancies for Na in the 3a site and for each TM in the 3b site are 1 and 0.25, respectively. Ordering between transition metals can be identified by neutron diffraction as the neutron scattering power depends on the coherent scattering length of an atom, not on its atomic number. As Ti, Fe, Co, and Ni have coherent scattering length of -3.44 , 2.49 , 9.45 , and 10.3 fm, respectively,^[18] TM ordering in the 3b site, if it exists, between Ti, Fe, and either Co or Ni, can therefore be identified by Rietveld refinement. We examined the neutron diffraction pattern in the low- Q region (the **Figure 1a** inset), where the TM ordering peaks would appear, and found no sign of any superstructure. The refined pattern of a structural model with random transition metal distribution agrees well with the observed one. Thus, we find that in-plane

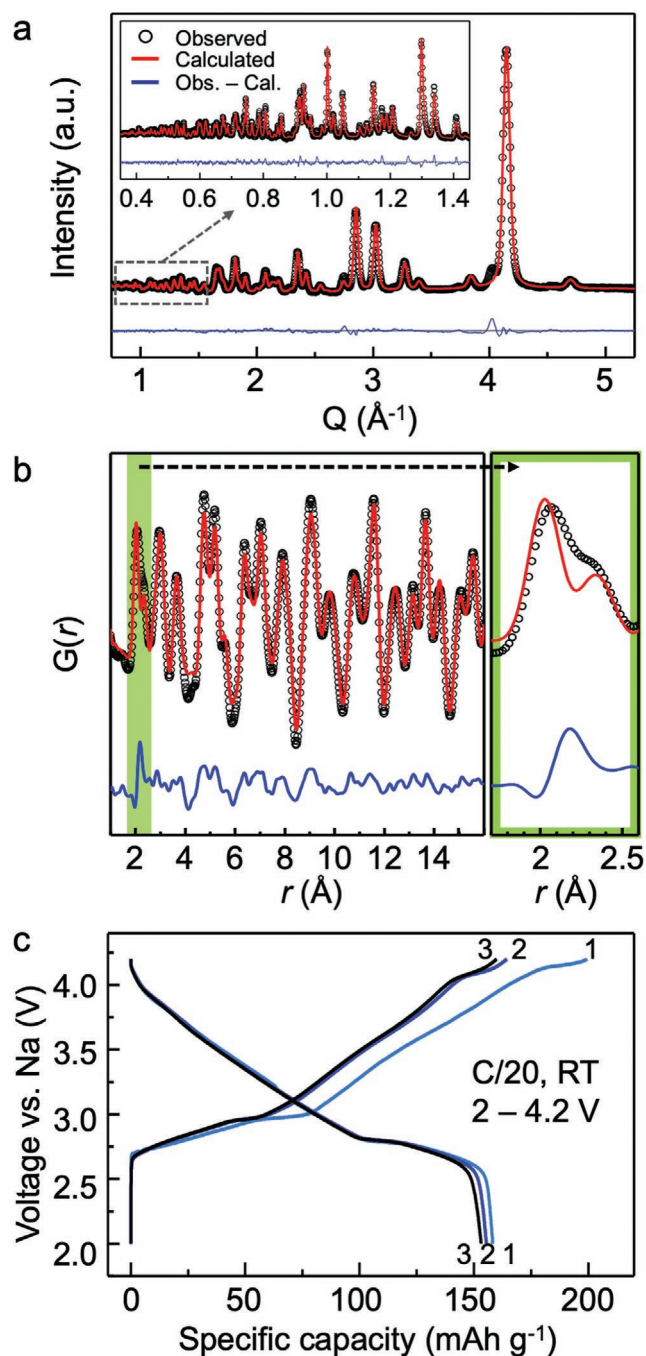


Figure 1. a) Neutron diffraction pattern and b) neutron pair-distribution function of as-synthesized $\text{NaTi}_{0.25}\text{Fe}_{0.25}\text{Co}_{0.25}\text{Ni}_{0.25}\text{O}_2$ (NaTFCN) with the right panel giving the detail for the low r region. c) The voltage–capacity profile of the NaTFCN cathode with respect to the Na metal anode for the first three cycles.

TM ordering is unlikely. Table S1 in the Supporting Information summarizes the refinement results.

Figure 1b shows the neutron PDF, which contains information about the local structure. The PDF result for large r (3.3–30 Å) could be fitted well using the same $R\bar{3}m$ model used for Rietveld refinement in **Figure 1a** (also shown in **Figure S1** in the Supporting Information), confirming that the bulk

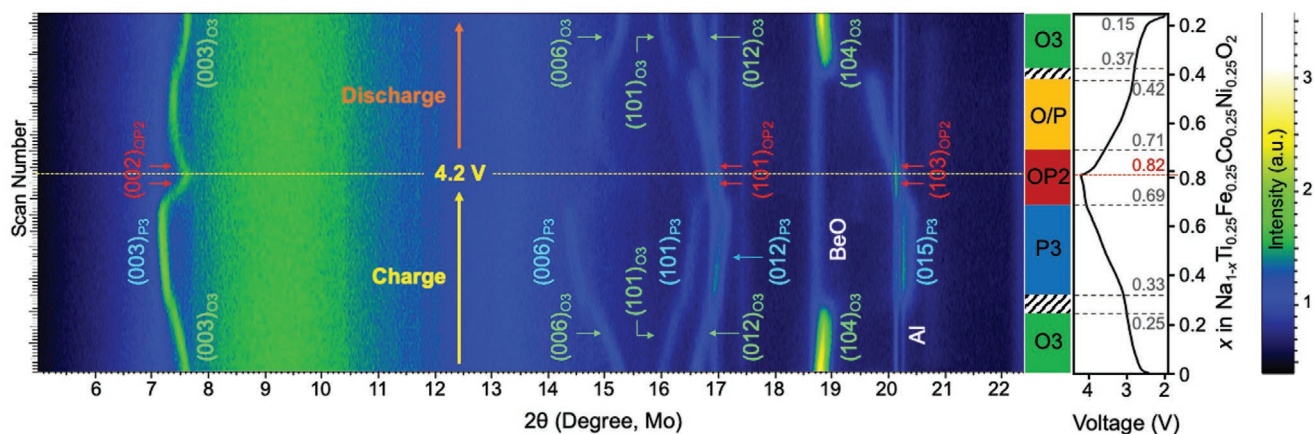


Figure 2. An intensity contour plot for the in situ XRD peaks of $\text{Na}_{1-x}\text{TFCN}$ in 2–4.2 V.

material has the O3-type stacking. Without changing the fitting parameters, we extended the fitting range to the small r region (1–3.3 Å) and found that the PDF data deviate from the calculated profile at ≈ 2 Å (the green-shaded region). This deviation is mostly due to the asymmetric shape of the first peak, which accounts for the TM–O bond length. The result implies that TM–O bond lengths have a significant deviation from their average value in NaTFCN. The local structural information according to the PDF analysis can be found in Table S2 in the Supporting Information.

Figure 1c shows the first three galvanostatic cycles of the NaTFCN cathode at C/20 ($1\text{C} = 242\text{ mA g}^{-1}$) at room temperature. The first charge and discharge capacities are 204 and 165 mAh g^{-1} , respectively. In subsequent cycles, the reversible capacity stabilizes at $\approx 160\text{ mAh g}^{-1}$. The first cycle capacity loss can be due to SEI formation, electrolyte decomposition, and/or the oxygen evolution at 4.2 V.^[19]

To better understand the Na (de)intercalation behavior of NaTFCN, we monitor the structure evolution as a function of the Na content upon charge and discharge in 2–4.2 V using in situ XRD. The result is shown in **Figure 2**. At $x = 0$ in $\text{Na}_{1-x}\text{Ti}_{0.25}\text{Fe}_{0.25}\text{Co}_{0.25}\text{Ni}_{0.25}\text{O}_2$ ($\text{Na}_{1-x}\text{TFCN}$), the XRD pattern shows the O3-type layered structure, characterized by the $(003)_{\text{O3}}$ and $(104)_{\text{O3}}$ peaks at 7.6° and 18.8° , respectively. Upon desodiation, the $(003)_{\text{O3}}$ peak shifts toward a lower angle in $0 < x < 0.25$, indicating c -lattice parameter expansion due to the increasing Na interlayer spacing. In the same region, the $(104)_{\text{O3}}$ peak shifts toward a higher angle as a result of decreasing in-plane TM–TM bond length, reflecting the oxidation of transition metals. As desodiation proceeds to $0.25 < x < 0.33$, the $(003)_{\text{O3}}$ peak position appears to change discontinuously, and the $(104)_{\text{O3}}$ peak vanishes. A new set of peaks appears near 7.3° and 20.3° , which belong to the P3-type structure indexed as $(003)_{\text{P3}}$ and $(015)_{\text{P3}}$, respectively. P3 has prismatic Na sites created by the octahedral TMO_6 slabs above and below, which repeat with a period of three (ABBCCA stacking). The continuous peak shifting for $0.33 < x < 0.69$ indicates that topotactic Na extraction occurs by a single-phase mechanism: the Na slab spacing gradually expands until the cell voltage reaches 4 V ($x = 0.69$).

Charging $\text{Na}_{1-x}\text{TFCN}$ into the region $0.69 < x < 0.82$ requires a potential higher than 4 V and leads to a peculiar structural

change. The $(003)_{\text{P3}}$ peak at 7.2° abruptly shifts toward higher 2θ , implying that the Na slab spacing collapses. New peaks also appear at 16.9° and 20.1° . In situ XRD could not fully reveal the structure due to the limited number of diffraction peaks, substantial peak broadening, as well as peak overlapping with the Al current collector of the cell. It should be emphasized that the structure at the end of charge can be fitted to neither the P3 nor the O3 structure model.

To identify the high voltage structure in atomic resolution, we employed high-angle annular dark-field (HAADF) STEM, in which the contrast is sensitive to the atomic number (Z) of periodic atoms in the sample ($Z^{-1.7}$).^[20] Three samples were prepared by electrochemical desodiation: pristine NaTFCN, $\text{Na}_{0.65}\text{TFCN}$ (charged to 3.3 V), and $\text{Na}_{0.22}\text{TFCN}$ (to 4.2 V). HR-STEM images for all samples were taken consistently in the same [100] direction.

In a pristine NaTFCN particle (**Figure 3a**), HR-STEM displays arrays of bright spots representing TM constituents (i.e., Ti, Fe, Co, and Ni) and dimmer spots corresponding to Na, visualizing the typical layered structure. **Figure 3b** shows the atomic arrangement of NaTFCN at a higher magnification. The interlayer distance, measured by the distance between transition metals in distinct layers, is 5.2 Å. The O3 unit cell with the $R3m$ symmetry overlaid onto the HR-STEM image matches well with the atomic arrays of Na and TM in NaTFCN. The simulated HR-STEM O3 result (inset in **Figure 3b**, white box) also reproduces the observed STEM image well.

Figure 3c,d shows HR-STEM images with low and high magnification obtained from desodiated $\text{Na}_{0.65}\text{TFCN}$. The arrays of bright spots correspond to the TM contrast. The P3 model structure with the $R3m$ symmetry (i.e., no inversion center) is projected onto the observed HR-STEM image in **Figure 3d**. The atomic positions of the TM layer in the P3 unit cell and the simulated HR-STEM image of the P3 structure (framed inset in **Figure 3d**) match well with the bright spots in the observed structure. The TM–TM interlayer distance is 5.7 Å. It should be noted that for the P3 structure the Na contrast in HR-STEM (both observed and simulated) is much less pronounced than that for O3. This weak Na contrast can be attributed to the disordering of Na over two distinct prismatic sites available in the P3 structure. From the electron beam direction [100], the

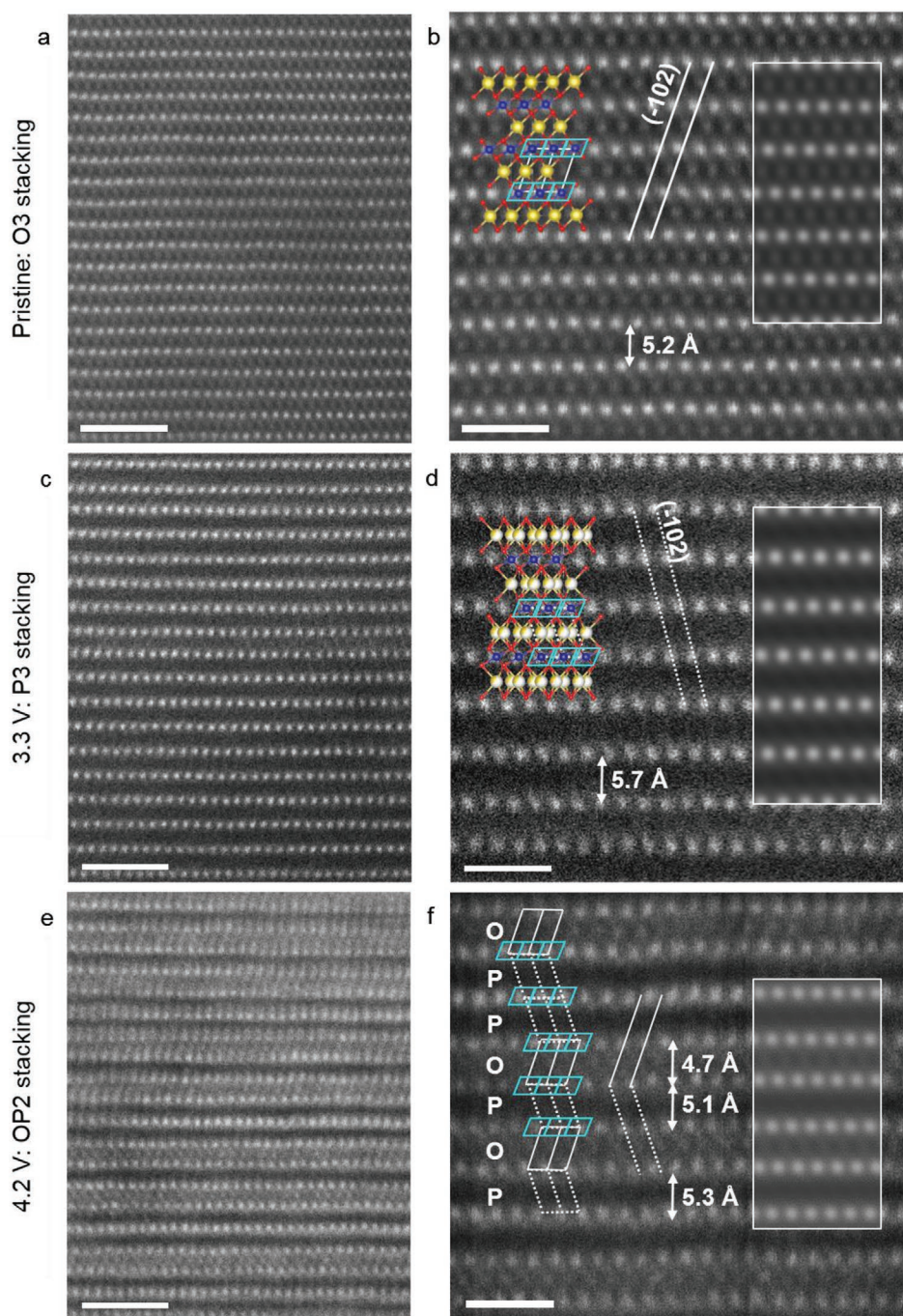
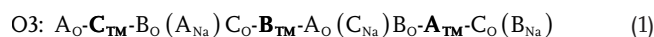
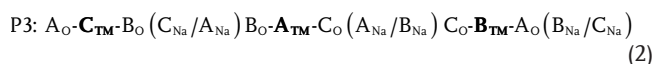


Figure 3. HR-STEM images obtained from $\text{Na}_{1-x}\text{TFCN}$ in three different states of charge: a,b) pristine with $x = 0$, c,d) charged to 3.3 V with $x = 0.35$, and e,f) charged to 4.2 V with $x = 0.78$. Simulated HR-STEM images using the multislice method with frozen phonon approximation are insets (white outline) in images (b), (d), and (f). (Scale bar: 2 nm in (a), (c), and (e); 1 nm in (b), (d), and (f).)

two prismatic Na positions do not coincide but overlap only slightly with one another (Figure S2, Supporting Information), resulting in a loss of intensity by a process known as the dechanneling effect.^[21,22] This effect of disordering is consistent with the simulation shown in the inset in Figure 3d, which also lacks intensity from the Na layer. Weak Na contrast is in fact one of the key features that differentiates P3 from O3 stacking and has been observed in other reports.^[23–28]

To explain the HR-STEM results obtained from $\text{Na}_{0.22}\text{TFCN}$ at 4.2 V charge (Figure 3e,f), we first describe O3 and P3 using the conventional nomenclature by which consecutive anion layers are labeled by their “A,” “B,” or “C” positions. O3 and P3 are then described by





where subscripts of O, TM, and Na indicate the position of the oxygen, transition metal, and Na layer. As Na in the P3 structure can occupy two different sites (face-sharing with the top/face-sharing with the bottom of a transition metal octahedron), we have labeled both. Most crucially, the bolded letters emphasize the transition metal layers, which are most visible in HR-STEM. By examining their order, the reversed stacking sequence of the transition metal layers becomes evident: O3 has $C_{\text{TM}}B_{\text{TM}}A_{\text{TM}}$ stacking while P3 has $A_{\text{TM}}B_{\text{TM}}C_{\text{TM}}$ stacking.

These reversed TM stacking sequences in the O3 and P3 structures can be seen in HR-STEM. In Figure 3b,d, we indicate TiO_6 octahedra (the blue rhombuses) to represent their orientations. As all the rhombuses for the O3 and P3 phases in HR-STEM are aligned in the same orientation, the TM stackings can be directly compared by looking at the $(\bar{1}02)$ plane that connects Na and TM in the O3 structure (the solid line in Figure 3b) and also in the P3 structure (the dashed line in Figure 3d). The $(\bar{1}02)$ orientation in the O3 structure is flipped compared with that in the P3 structure, depicting that the TM stacking sequence is reversed.

HR-STEM images with low and high magnifications from highly desodiated $\text{Na}_{0.22}\text{TFCN}$ (4.2 V) are shown in Figure 3e,f. The intensity from transition metals is clearly observable and shows that the structure remains layered at 4.2 V, although there is some rippling that is not seen in the O3 and P3 HR-STEM images. Unlike in the HR-STEM images in Figure 3a–d, we observe that the bright and dark contrasts from the Na layers alternate. In addition, no single line connecting transition metals can extend more than two slabs, indicating that the stacking sequence represents neither O3 or P3 (or O1).

Rather, we infer from the HR-STEM that two different types of stacking sequences alternate in the sample at 4.2 V. In Figure 3f, we note two different interlayer distances. TM–TM interlayer distances around bright (octahedral) and dark (prismatic) Na layers are 4.7 and 5.1 Å, respectively. The appearance of Na contrast in the bright layer indicates the stacking is octahedral, and the solid line tracing the transition metal and Na columns corresponds to the $(\bar{1}02)$ plane of the O3 structure. In the dark Na layer the stacking is displaced from $(C_{\text{TM}}B_{\text{TM}}A_{\text{TM}})$, where it would be if O3 continued, to $(C_{\text{TM}}B_{\text{TM}}C_{\text{TM}})$. This section is represented by the dashed line corresponding to the $(\bar{1}02)$ plane of the P3 structure (where noted by P). As previously explained, there is no Na contrast in this layer. Therefore, the dark Na layers are assigned to be prismatic stacking. The simulated HR-STEM image of $\text{Na}_{0.22}\text{Ti}_{0.25}\text{Fe}_{0.25}\text{Co}_{0.25}\text{Ni}_{0.25}\text{O}_2$ with alternating octahedral and prismatic stacking (inset, white box in Figure 3f) reproduces Figure 3f well, further corroborating these results.

As illustrated, the direction of the $(\bar{1}02)$ plane can be used to characterize the relative displacement of the transition metal slabs with respect to each other. In Figure 3f, the $(\bar{1}02)$ planes change direction consistent with changes in the contrast of Na layers in O and P. Indeed, this reversal of the $(\bar{1}02)$ plane indicates that TM–O bonding directions, exhibited by the blue rhombuses alternate between the directions presented for pure O3 and P3 (Figure 3b,d). This analysis of the HR-STEM data

indicates that the high voltage structure is formed by a regular gliding of TM–O slab. Note that while the $(\bar{1}02)$ plane is used to describe the features of structures, other planes could have been chosen. The dark/bright contrast variations characteristic of alternating P and O environments for Na appears striped can be unambiguously observed in a lower magnification in Figure S3 in the Supporting Information. On occasion two subsequent prismatic layers can also be observed (Figure S4, Supporting Information). When two prismatic stacking sequences are adjacent, the interlayer distance is larger at around ≈ 5.3 Å. Because the $\text{Na}_{0.22}\text{TFCN}$ high voltage structure exhibits alternating octahedral and prismatic stacking we refer to the structure as OP2, as suggested by Yabuuchi et al.^[12]

Now that the high voltage structure is identified, the evolution of the OP2 upon resodiation can be reexamined in Figure 2. Na insertion at 4.2 V causes the $(002)_{\text{OP2}}$ peak at 76° to shift to lower angles for Na content $0.82 > x > 0.71$ in $\text{Na}_{1-x}\text{TFCN}$, indicating that the *c*-lattice parameter increases. Concurrently, the $(101)_{\text{OP2}}$ and $(103)_{\text{OP2}}$ peaks at 16.9° and 20.1° slightly change to the lower angles. The downshift of the $(002)_{\text{OP2}}$ peak continues for $0.71 > x > 0.5$ to lower angle but stagnates around 74° at $x \approx 0.5$. As sodiation continues, the $(002)_{\text{OP2}}$ peak then shifts gradually to higher angle for $0.5 < x < 0.42$. Over this whole range $0.71 > x > 0.42$, the $(101)_{\text{OP2}}$ and $(103)_{\text{OP2}}$ peaks continuously shift to 16.6° and 19.7° , respectively. It is surprising that upon discharge the $\text{Na}_{1-x}\text{TFCN}$ phase does not show the characteristic set of peaks for O3 or P3 in the range $0.71 > x > 0.42$ as P3 mostly appears in this composition range during charge. Rather, the in situ XRD patterns confirms the continuous presence of OP2 with the $(002)_{\text{OP2}}$, $(101)_{\text{OP2}}$, and $(103)_{\text{OP2}}$ all substantially shifting from their position in the highly charged state at $x = 0.82$. In the region $0.42 > x > 0.37$ strong $(003)_{\text{O3}}$ and $(104)_{\text{O3}}$ peaks at 75° and 19° indicating that the O3 phase reappears via a two-phase reaction. Further sodiation leads the $(003)_{\text{O3}}$ peak to shift to 76° and the $(104)_{\text{O3}}$ peak to 18.8° at the end of discharge ($x = 0.15$). To summarize, $\text{Na}_{1-x}\text{TFCN}$ undergoes an O3–P3–OP2 phase transition upon charge between 2.5 and 4.2 V, but upon discharge the OP2 structure bypasses the P3 phase and transforms directly to the O3 phase.

Using XAS, we investigate the redox reactions in the quaternary transition metals during the first charge and discharge and their relation to the local environment changes around different transition metals. Twelve ex situ XAS samples were prepared electrochemically (1 pristine, 6 different states of charge, and 5 different states of discharge) at conditions shown on the voltage profile in Figure S5 in the Supporting Information. XAS upon TM oxidation is shown in Figure 4. XAS upon TM reduction can be found in Figure S6 in the Supporting Information but is essentially the same (in reverse) as in charge.

Figure 4a–d shows X-ray absorption near edge structure (XANES) of Ti, Fe, Co, and Ni in NaTFCN at different states of charge. For pristine NaTFCN (sample 0), the oxidation states of each transition metal were previously determined as Ti^{4+} , Fe^{3+} , Co^{3+} , and Ni^{2+} .^[16,17] In Figure 4a, the Ti K-edge during charging is invariant, indicating that Ti is electrochemically inert between 2.5 and 4.2 V. However, the Ti pre-edge changes noticeably at the end of charge at 4.2 V (sample 6), suggesting that TiO_6 octahedra undergo substantial distortion. The Fe K-edge in Figure 4b does not shift in the range 2.5–3.25 V (samples 0–3),

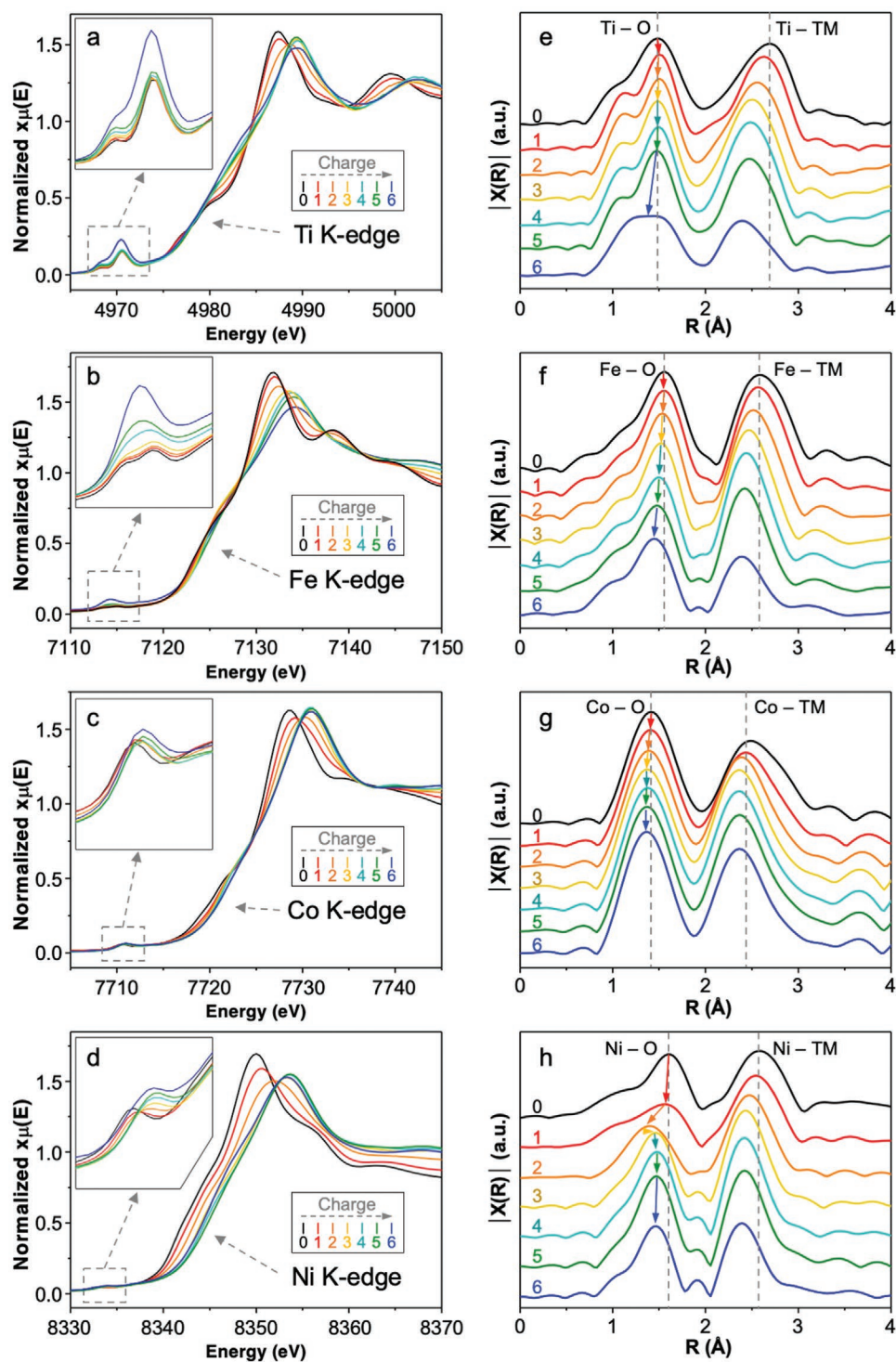


Figure 4. Ex situ XAS for the quaternary transition metals upon charging. XANES for a) Ti, b) Fe, c) Co, and d) Ni, and EXAFS for e) Ti, f) Fe, g) Co, and h) Ni. Samples 0, 1, 2, 3, 4, 5, and 6 are prepared by electrochemical desodiation from NaTFCN, in which the capacities are 0, 35, 71, 106, 141, 176, and 209 mAh g⁻¹, respectively.

but Fe oxidation is observed at high voltage between 3.25 and 4.2 V, (samples 4–6). Its contribution to the overall capacity is small as the edge shifts only slightly to higher energy.^[12] We also observe a change in the pre-edge of Fe at high state of charge,

suggesting its environment becomes distorted. The Co K-edge is shown in Figure 4c and shifts at low voltage (samples 0–3) but not in the high voltage region (samples 4–6), indicating that Co oxidation compensates for desodiation at low state of charge.

Figure 4d shows a substantial shift in the Ni K-edge, suggesting oxidation occurring over the whole voltage range (2–4.2 V). In summary, Ni²⁺ and Co³⁺ oxidize first at low voltage, followed by Ni³⁺ and some Fe³⁺ oxidation at high voltage. On discharge, the redox couples are reduced in the opposite order as on charging (Figure S6, Supporting Information).

Figure 4e–h shows the extended X-ray absorption fine structure (EXAFS) spectra of Ti, Fe, Co, and Ni for the same states of charge as used in Figure 4a–d. (Results for discharge can be found in Figure S6 in the Supporting Information.) EXAFS gives element-specific information for the TM–O and TM–TM local environment. The EXAFS in Figure 4e indicate that Ti–O bond length does not change in samples 0 to 5 (2.5–3.9 V), further supporting that Ti is not involved in the electrochemical reaction. The Ti–TM bond length becomes shorter upon desodiation due to the oxidation of other TMs. At the end of charging (sample 6) both the Ti–O and Ti–TM bond lengths decrease abruptly while their EXAFS signals broaden and intensities decrease, indicating a substantial distortion of the O_h point symmetry of the TiO₆ octahedron. Figure S6e in the Supporting Information shows that Ti recovers its octahedral symmetry upon discharge. The EXAFS spectra for Fe in Figure 4f show that the Fe–O bond length is invariant at low desodiation level (samples 0–3, 2.5–3.25 V) but shortens upon higher charge, concomitant with a decrease of EXAFS intensity. At the end of charging (4.2 V), the Fe–O and Fe–TM bond lengths abruptly decrease and the related EXAFS intensity weakens. These changes are consistent with oxidation to Fe⁴⁺. The strong Jahn–Teller activity of Fe⁴⁺ lowers the symmetry around the ion leading to a reduction of peak intensity.^[29] The peak and intensity changes for Fe are reversible as resodiation removes the local distortion around Fe and recovers the octahedral symmetry (Figure S6f, Supporting Information). Consistent with the XANES data, the EXAFS spectra in Figure 4g indicate that the Co–O and Co–TM bond lengths only decrease at low voltage (samples 0–3, 2.5–3.25 V), indicating Co oxidation. Unlike the cases of Ti and Fe, the EXAFS intensities for Co–O and Co–TM remain unchanged consistent with Co³⁺ and Co⁴⁺ preferring an almost ideal octahedral environment around them.^[30,31] The EXAFS data for Ni, shown in Figure 4h, is consistent with its oxidation to Ni²⁺ and Ni⁴⁺ in charging. For samples 0–2, charged between 2.5 and 3 V, the EXAFS intensity and Ni–O bond length decrease due to the Jahn–Teller distortion of Ni³⁺. Upon further desodiation (samples 3–5, 3.25–3.9 V), this intensity increases, consistent with recovery of octahedral symmetry around Ni⁴⁺. At the end of desodiation, the EXAFS intensity slightly decreases again, likely due to the interaction with other TM such as Ti and Fe, which is commonly observed in layered oxide cathodes.^[19,32] In summary, the TiO₆ and FeO₆ octahedra are distorted at high state of charge. The Co–O environment is invariant throughout desodiation. The Ni–O environment undergoes distortion at intermediate desodiation, recovers its octahedral symmetry, and then distorts again at high state of charge.

To understand better why OP2 forms we use first-principles computations to investigate a model system containing only Fe^{3+/4+} and Ni^{3+/4+} ions as these are the active ions in the highly charged state. We calculate the energy of the different structures that can be obtained by slab-gliding from the O3 structure

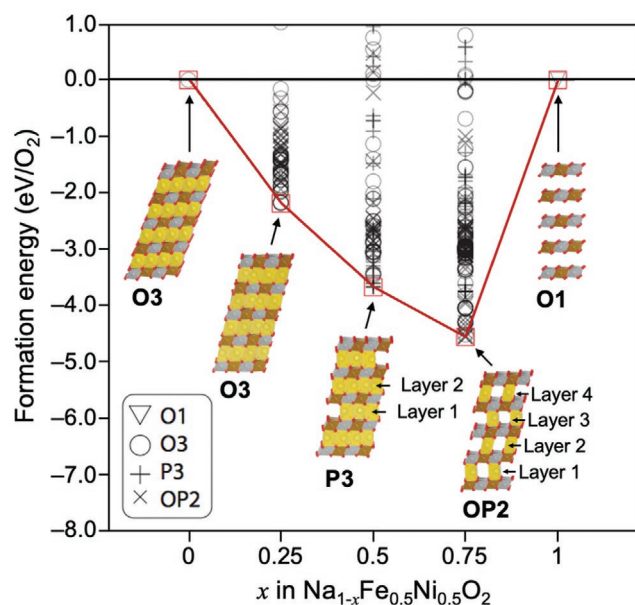


Figure 5. Formation energies of O3, P3, OP2, and O1 structures as a function of the Na content in Na_{1-x}Fe_{0.5}Ni_{0.5}O₂ (convex-hull construction) and the ground state orderings at $x = 0, 0.25, 0.5, 0.75,$ and 1 .

(O3, P3, OP2, and O1). For each of these, several hundred Na-vacancy orderings at different Na compositions are evaluated as described in the Experimental Section. Figure 5 shows formation energies as a function of the Na content in Na_{1-x}Fe_{0.5}Ni_{0.5}O₂ ($x = 0, 0.25, 0.5, 0.75,$ and 1). Thermodynamically stable structures, based on the convex-hull construction,^[33,34] are boxed in red, indicating that; at $x = 0$ and 0.25 , the ground state structure is O3 (circle), at $x = 0.5$, the structure is P3 (plus), and at $x = 0.75$, the structure is OP2 (cross). The ground state of the fully desodiated endpoint, at $x = 1$, is the O1 phase (triangle). These 0 K ground states, illustrated in Figure 5 and described in Table 1, are also maintained at 300 K (see Figure S7 in the Supporting Information) when the free energy includes a simple ideal-solution-like approximation for the configurational entropy.

Table 1 summarizes the Na coordination environment and average TM–TM interlayer distance in O3, P3, and OP2 ground state structures on the hull from Figure 5. Note that the TM–TM interlayer distance refers to the vertical distance from one TM layer to another. The effective Na content is listed when there are multiple layers within the unit cell. The ground state structures are geometrically optimized using strongly constrained and appropriately normed (SCAN) functional, which has been shown to reproduce known experimental lattice parameters more accurately than the Perdew–Burke–Erzenhof (PBE) functional.^[35] Recent work observed that the SCAN functional includes medium-range intermediate van der Waals forces without compromising known thermodynamic stability rules and so in this case does not systematically over-stabilize features such as larger c -lattice parameters.^[36]

Consistent with the experimental result, a transition occurs from a stable O3-type structure a large Na concentration to the P3 structure around $x \approx 0.5$. The lowest energy calculated P3 structure at $x = 0.5$ contains 0.375 Na in one layer and 0.625

Table 1. Description of Na occupancies and lattice parameters in the lowest energy phases calculated by SCAN.

x	Stable structure	Na layer	Na environment	Na content	TM–TM interlayer distance [Å]
0	O3	All	Octahedral	1	5.44
0.25	O3	All	Octahedral	0.75	5.50
0.5	P3	Layer 1	Prismatic	0.375	5.91
		Layer 2	Prismatic	0.625	5.85
0.75	OP2	Layer 1	Prismatic	0.25	5.80
		Layer 2	Octahedral	0.25	5.77
		Layer 3	Prismatic	0.25	5.79
		Layer 4	Octahedral	0.25	5.77
1	O1	All	N/A	0	4.52

in the next. The OP2 ground state structure at $x = 0.75$ in $\text{Na}_{1-x}\text{Fe}_{0.5}\text{Ni}_{0.5}\text{O}_2$ has an even distribution of Na in the layers. The O1-type structure identified by computation is similar to what is found in some fully desodiated layered TMO_2 .^[37]

According to the results in Table 1, the average slab spacing in O3 increases from 5.44 to 5.50 Å upon desodiation to $x = 0.25$, further increases to 5.88 Å when the P3 phase becomes stable at $x = 0.5$ in $\text{Na}_{1-x}\text{Fe}_{0.5}\text{Ni}_{0.5}\text{O}_2$, and decrease to 5.78 Å in the OP2 phase at $x = 0.75$. These slab height changes are qualitatively consistent with the experimental results shown in Figures 2 and 3. Using the calculated structures, we generated XRD patterns for the O3, P3, and OP2 ground states and compare them with ex situ XRD patterns with the corresponding Na content, as shown in Figure S8 in the Supporting Information. The simulation captures the observed lattice parameter changes during charging well.

3. Discussion

In this paper we provided evidence for the appearance of the OP2 phase at the top of charge in NaTFCN and directly visualized the structure using HR-STEM. This structure is highly unusual as it periodically repeats alternating O and P stacking leading to a unit cell length along the c -axis of ≈ 16.2 Å. The fact that a periodic structure of O and P blocks is stable rather than a phase separation between distinct O and P phases indicates that some physical effect provides a positive interaction between the O and P layers at this composition. The EXAFS data suggest that it is associated with strong distortions around the Ni, Ti, and Fe site. Other factors correlating with its stability can be gleaned from the chemistries for which OP2 occurs such as $\text{Na}_{1-x}\text{Mn}_{0.5}\text{Fe}_{0.5}$ and $\text{Na}_{1-x}\text{Mn}_{0.4}\text{Fe}_{0.2}\text{Ni}_{0.4}$ for large x .^[12,13] But not all layered Na compounds display an OP2 structure at high state of charge. For example, in $\text{NaMn}_{0.25}\text{Fe}_{0.25}\text{Co}_{0.25}\text{Ni}_{0.25}\text{O}_2$ the O3–P3–O3 phase transition is observed rather than O3–P3–OP2.^[38] To rationalize these different observations, we analyze how the Na–O–TM interactions affect the OP2 phase stability at Na = 0.25. In Figure S9 and Description S9 in the Supporting Information, we show arguments why these are the most likely interactions responsible for OP2's stability.

The concentration at which OP2 forms coincides with the formation of Fe^{4+} , as demonstrated by in situ XRD (Figure 2) and ex situ XAS (Figure 4). The e_g -level degeneracy of high-spin

Fe^{4+} in FeO_6 octahedra causes a strong JT distortion, buckling the layered structure.^[39] We demonstrate here that this JT activity is crucial for forming OP2. Note that the P3 phase, rather than OP2, is observed above 4 V in various Fe-free Ni-containing NaTMO_2 ,^[13,40,41] suggesting that OP2 stabilization at high state of charge by Ni^{3+} is less likely. This is consistent with the fact that the Ni^{3+} JT distortion is considerably weaker than for Mn^{3+} and Fe^{4+} and the fact that much of Ni^{3+} is oxidized to the non-JT-active Ni^{4+} .

A JT ion, in essence, enables a transition metal octahedron to distort while lowering the electronic energy of the metal. For example, the Q3 JT mode by which one octahedral axis becomes longer and the other two become shorter can be oriented along any of the three octahedral axes,^[42] enabling a degree of freedom whereby any of the faces of the oxygen octahedron can be displaced at no energy cost in order to satisfy the interaction of those oxygen ions with other ions. Connectivity of a Na ion to the long axis of the JT ion Fe^{4+} , via the intermediate O anion, thus also affords the Na an additional degree of freedom in an otherwise highly constrained environment. This is because the size of the triangular base of the prism or octahedron is controlled by the size of the transition metal, leaving only the slab spacing adjustable for Na to optimize its sixfold coordination.

We thus consider the influence of the long axis of the oxygen octahedron around the JT Fe^{4+} ion on Na–O bonds in all OP2 structures ($n = 7$) which are within 50 meV per O_2 above the sodiation hull. Figure 6a shows the normed distribution of Na–O bond lengths categorized by the connectivity of its bound O anion, which can be to either the long axis of the JT ion (indicated by $\text{Fe}^{4+}_{\text{JT}}$, in red) or not (in gray). The histogram shows how the Fe^{4+} JT distortion accommodates shorter Na–O bond lengths compared to those formed by a non-JT-ion. This effect is also observed in all other competitive structures less than 50 meV per O_2 above the hull (Figure S10, Supporting Information). We reason that the shorter Na–O bond made possible by $\text{Fe}^{4+}_{\text{JT}}$ improves the effective coordination of Na. (See Description S10 in the Supporting Information for discussion on the ideal Na–O bond length in NaO_6 sixfold environments.) As a result, this optimization of Na coordination leads to a preference for Na–O– $\text{Fe}^{4+}_{\text{JT}}$ triplets in which the long-axis of the Fe^{4+} JT bond is connected to Na. Figure 6b illustrates one such Na–O– $\text{Fe}^{4+}_{\text{JT}}$ triplet in green, showing how the long axis of the JT ion extends its O anion into the Na octahedral (prismatic)

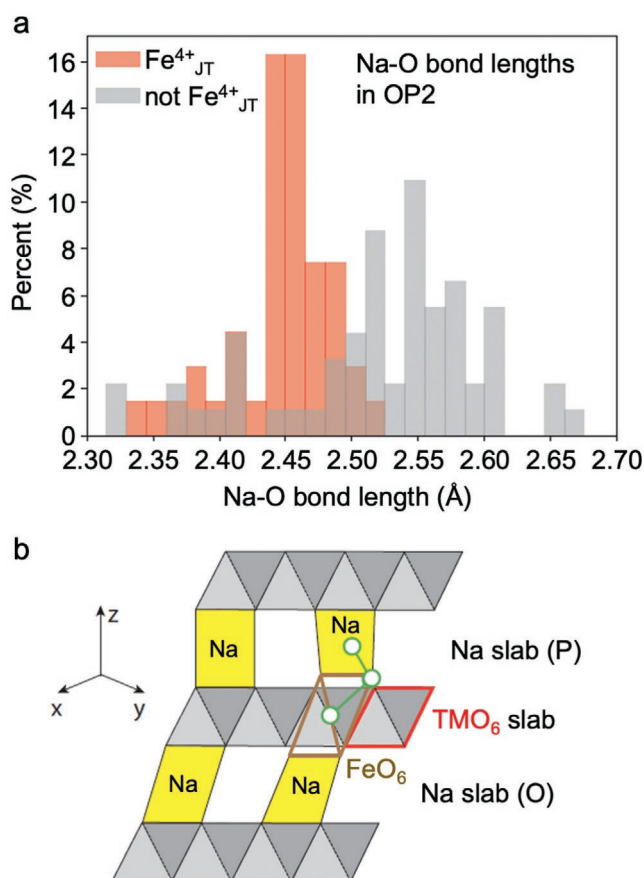


Figure 6. a) Normed histogram of Na–O bond lengths in seven OP2 structures, which are within 50 meV per O_2 above the sodiation hull. Red indicates the Na–O bond is connected to long axis of the Jahn–Teller active Fe^{4+}_{JT} while gray indicates an alternate connection (e.g., short axis of the Jahn–Teller active Fe^{4+} ion, or any bond with Ni^{3+} or Ni^{4+}). b) Schematic of an $Fe^{4+}O_6$ octahedron in OP2. The $Fe^{4+}O_6$ octahedron (brown outline) next to non-Jahn–Teller-activated TMO_6 octahedron (red outline) is shown to interact with prismatic and octahedral Na. The green three-atom cluster indicates the favorable Na–O– Fe^{4+} triplet interaction.

slab, thereby reducing strain on the edge-sharing octahedral (prismatic) site below (above). In summary, we reason that a Jahn–Teller ion, such as Fe^{4+} is effectively a way to distort the underlying TM-octahedron at no energy cost and enables the system to lower its energy by improving the effective coordination for Na.

If the Na–O– Fe^{4+}_{JT} triplet is the favored Na–O–TM triplet, then we hypothesize that OP2 accommodates the greatest number of such triplets. **Figure 7a** illustrates this interaction in an example OP2 structure. An oxygen atom that is part of the octahedral coordination around the Na atom is connected to a Jahn–Teller-activated Fe^{4+} arm. This connectivity thus forms the Na–O– Fe^{4+}_{JT} triplet as circled in bold black lines.

To test our hypothesis, we carry out a simulation to investigate which of the three stacking sequences accommodates the highest probability of Na–O– Fe^{4+}_{JT} triplets. The description of the cell sizes used and structure generation algorithms are given in the Experimental Section. We assume each structure contains 25% randomly distributed Fe^{4+} , in which one pair

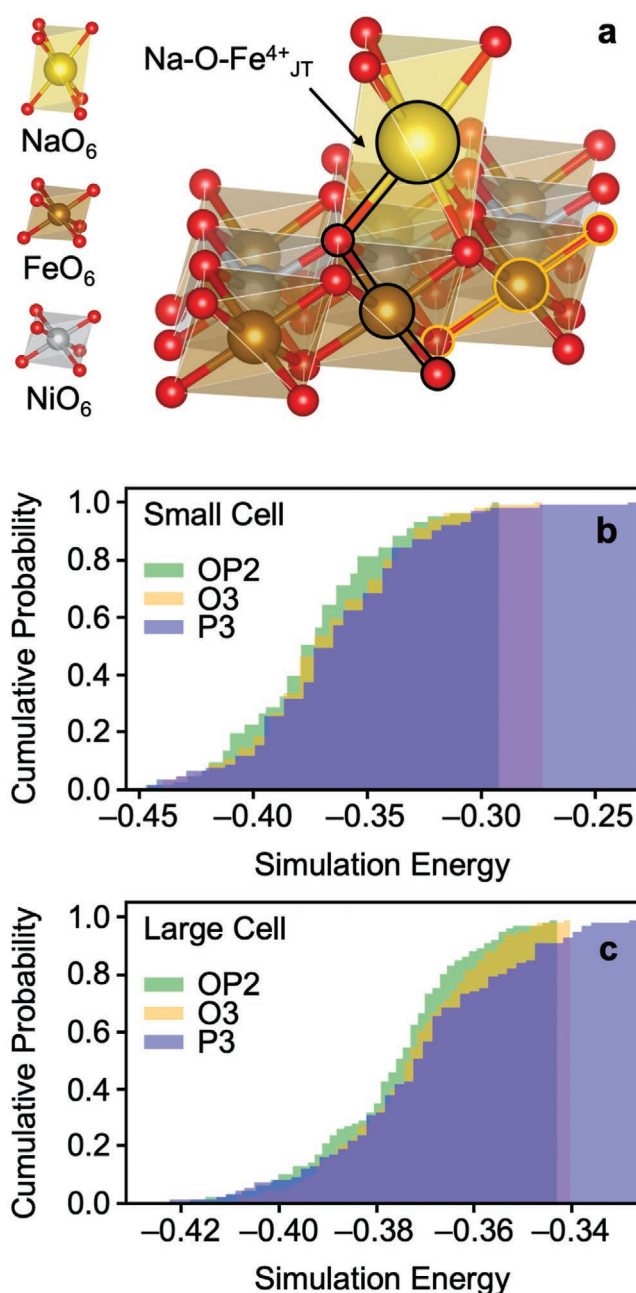


Figure 7. a) Na–O– Fe^{4+}_{JT} triplet marked by black lines in the OP2 structure (a single Na atom in a P3 layer is shown for clarity). Jahn–Teller modes across different Fe^{4+} (indicated by orange lines) are not assumed to be correlated. b) The cumulative probability of having Na–O– Fe^{4+}_{JT} triplets in a small cell and c) in a large cell.

of axial bonds in each FeO_6 is designated as the long Jahn–Teller Fe^{4+} –O bond. Na ions are also randomly distributed. If the activated Fe^{4+}_{JT} is connected to Na, it is referenced in the simulation as a stabilizing interaction and assigned a unitless energy of -1 . Note that 1) one O is always connected to three transition metals, so as long as one of these connections is Na–O– Fe^{4+}_{JT} , we consider the Na–O bond to be a Na–O– Fe^{4+}_{JT} triplet. The maximum number of Na–O– Fe^{4+}_{JT} connections

per Na atom is six. 2) The overall Na content of the test structures is constrained to 0.25 but no requirement that each layer contains the same concentration is imposed. Finally, the total number of Na–O–Fe⁴⁺_{JT} triplets is normalized per formula unit (Na_{0.25}M_{0.5}Fe_{0.5}O₂), yielding the normalized unitless simulation energy shown in Figure 7b,c for small and large cells, respectively.

Since the cumulative probability illustrates which structure type has the greatest number of stabilizing Na–O–Fe⁴⁺_{JT} triplets, it also indicates which stacking has the greatest number of lower-energy arrangements of the ions. We observe that regardless of cell size, the OP2 structure has the greatest probability of low energy structures precisely due to its greatest number of Na–O–Fe⁴⁺_{JT} triplets. In summary, by enumerating structures with fully randomized Na and TM occupancy, with no assumption about Na–Na interactions or correlated Fe Jahn–Teller modes, we find evidence that the OP2-type stacking indeed affords the greatest number of connections between Na and Jahn–Teller-activated Fe⁴⁺.

It should be pointed out that even though NaMn_{0.25}Fe_{0.25}Co_{0.25}Ni_{0.25}O₂ contains Fe⁴⁺, it goes through an O3–P3–O3 phase transition, without an OP2 phase appearing.^[38] The difference between this composition and ours suggests that Ti⁴⁺ may also play a role in relieving the strain needed to adjust the Na coordination. This is not surprising since Ti⁴⁺ is a d⁰ element, which has been shown to accommodate highly distorted octahedral sites because it lacks the valence electrons that induce preference for certain bond geometries.^[43,44] XANES results shown in Figure 4 indicate indeed that octahedral TiO₆ is strongly distorted upon Fe oxidation. The electronic structure of Ti may therefore facilitate the displacement of oxygen ions to improve the Na coordination.

We also remark on the relatively low Fe concentration in NaTFCN, which is notably below the Fe doping threshold of 30% as proposed by Li et al. to suppress Fe migration.^[29] They argued that locally rich Fe clusters lower the energy barrier for Fe migration into tetrahedral sites. Consistent with that threshold, we do not observe any sign of Fe migration in desodiated NaTFCN by STEM analysis. Therefore, we emphasize that using Fe is a sensible approach for designing NaTMO₂ with reversible phase transformations and greater cyclability. Solutions that rely on an even higher Fe concentration would be highly valuable.

P3 and OP2 are stable at the intermediate ($x = 0.5$) and low ($x = 0.75$) Na content, respectively, in Na_{1-x}TFCN, leading to the O3–P3–OP2 phase transition upon desodiation. However, the observation that the P3 phase does not appear upon resodiation, as shown in Figure 2, implies that the formation of OP2 triggers different phase transformation paths upon discharge from those on charge. We speculate that the difference in desodiation and resodiation pathways arises from the Na intercalation kinetics in O and P layers. Na ions diffuse faster through face-sharing prismatic sites than through edge-sharing octahedral sites.^[45] One piece of evidence may be found in the different behavior of the *c*-lattice parameter in charge and in discharge.

Figure 8 replots the (00*l*) peaks from Figure 2. The *c*-lattice parameter of Na_{1-x}TFCN approximately at $x = 0.7$ in discharge is much smaller than at $x = 0.7$ in charge (red circles). This

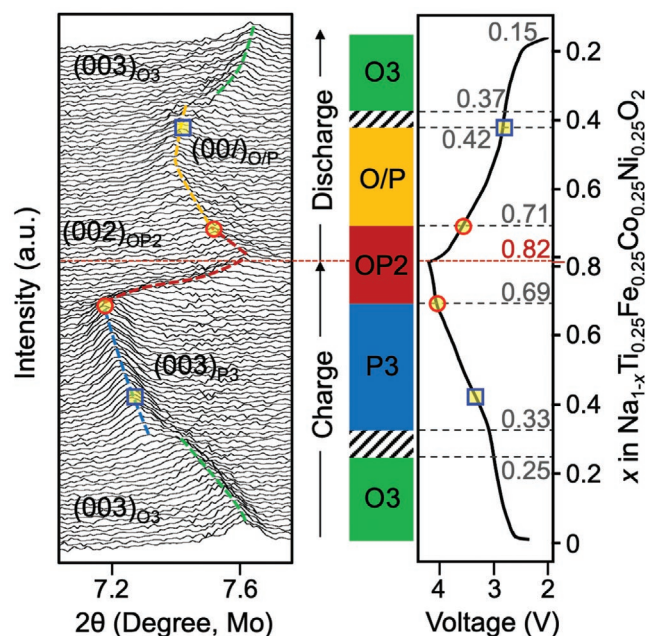


Figure 8. In situ XRD for (00*l*) peak evolution as a function of the Na content.

suggests that the discharging structure remains “collapsed” as the OP2 phase and does not form P3. By carefully inspecting in situ XRD upon discharge, we found that there are three different stages for the (00*l*) peak shift. The peak shifts to lower angle from 762° to 751° in 0.71 < x < 0.82 and from 751° to 74° in 0.5 < x < 0.71, but to higher angle from 74° to 745° in 0.42 < x < 0.5, suggesting three different modes of *c*-lattice parameter variation.

While equal Na occupancy is predicted in the O and P layers at equilibrium, sodiation into the O layer may occur kinetically faster than sodiation into the P layer. As a result, the Na slab spacing of the O and P layers in the OP2 phase may change at different rates. During the early resodiation stage, for 0.82 > x > 0.71, while the OP2 structure is maintained, the P slab spacing is seen to increase faster than the O slab spacing. As sodiation continues, the slab spacing of the P layer which contains more Na than that of the O layer will start to decrease due to the reduced interlayer Coulombic repulsion, whereas the slab spacing for the O layer increases due to its lower population of Na. This may lead to the stagnated *c*-lattice parameter change that is observed for 0.71 > x > 0.5. For 0.5 > x > 0.42, the *c*-lattice parameter gradually decreases as more Na in the O layers can now screen the Coulombic repulsion. When $x = 0.42$ is reached in discharge, the *c*-lattice parameter of the discharged phase is still smaller than that of the charged P3 phase at $x = 0.42$ (blue squares). It is possible that the OP2 structure starts to develop faults as P layers turn into O layers when they have reached a high Na content. This defected structure finally turns into the O3 phase through a two-phase reaction between 0.42 > x > 0.37. We note that in spite of the path-dependent Na (de)intercalation, the O3 phase is reasonably recovered at Na_{0.85}TFCN after the first discharge.^[29]

In summary, the difference in desodiation and resodiation pathway is consistent with the more rapid Na intercalation

in the P layers of the OP2 phase. We consider that this coordination-dependent Na mobility causes the P layers to transform to O before the O layers absorb enough Na to transform to P, kinetically suppressing the formation of the P3 phase upon discharge. While the voltage versus capacity profile of NaTFCN upon charge and discharge is asymmetric, the O3 phase is recovered in the discharged structure and can sustain reversible Na extraction and insertion in subsequent cycles.

4. Conclusion

We directly observe and rationalize the formation of a new phase called OP2, consisting of alternating octahedral–prismatic oxygen stacking, which is formed at a high state of charge in the O3-NaTi_{0.25}Fe_{0.25}Co_{0.25}Ni_{0.25}O₂ cathode. The redox process is highly reversible after the first cycle and generates a specific capacity of ≈160 mAh g⁻¹ when charged to 4.2 V. We suggest that the OP2 phase is thermodynamically stable due to the local optimization of oxygen coordination around Na enabled by Jahn–Teller active Fe⁴⁺ and distortion-tolerant Ti⁴⁺. As layered Na transition metal oxide cathodes utilizing a large amount of Fe are known to face stability challenges, it is remarkable that a specific concentration of Fe, ensuring oxidation to Fe⁴⁺, remains redox-active while undergoing complex phase transitions. Therefore, we hope to motivate future studies in layered Na-cathodes that incorporate some fraction of Fe as a crucial mechanical stabilization ingredient, enabling stability at higher charge and achieving greater intercalation in Na-ion batteries.

5. Experimental and Computational Section

Synthesis: To obtain the target composition, 20% excess Na₂O (80%, Alfa Aesar) was combined with stoichiometric amounts of TiO₂ (99%, Sigma-Aldrich), Fe₂O₃ (99%, Sigma-Aldrich), Co₃O₄ (99%, Alfa Aesar), and NiO (99%, Alfa Aesar). The precursors were mixed with a SPEX 8000M Mixer/Mill in an argon-filled glovebox for 1 h. The resulting mixture was pressed into a disc-shaped pellet, fired at 800 °C for 10 h under flowing oxygen, and quenched to room temperature. The sample was transferred into the glovebox immediately after quenching to minimize air-exposure.

Structural Characterization: To analyze the structure of as-synthesized materials, time-of-flight (TOF) powder neutron diffraction patterns were collected at room temperature on the nanoscale ordered materials diffractometer (NOMAD) in the Spallation Neutron Source at Oak Ridge National Laboratory and analyzed by Rietveld refinement using a TOPAS 4.2 software package. The PDF data was fitted using a PDFGUI software.^[46] The samples were sealed in a quartz tube in an Ar-filled glovebox.

XAS: XAS was carried out at the MRCAT 10-ID beamline in the Advanced Photon Source (APS), Argonne National Laboratory. K-edges of Ti, Fe, Co, and Ni spectra were recorded in transmission mode at room temperature with a SiO₂ monochromator. For XAS sample preparation, NaTi_{0.25}Fe_{0.25}Co_{0.25}Ni_{0.25}O₂, carbon black (Timcal, Super P), and polytetrafluoroethylene (PTFE, DuPont) were mixed and rolled into a film and sealed with a Kapton tape. The XANES and EXAFS spectra were analyzed using Athena and Artemis software, respectively.

Battery Test: The cathode film was made of 80 wt% NaTi_{0.25}Fe_{0.25}Co_{0.25}Ni_{0.25}O₂, 15 wt% carbon black, and 5 wt% PTFE with a loading density of ≈3 mg cm⁻². A 2032-coin cell was assembled with the cathode film, Na metal (Sigma-Aldrich) as an anode, ethylene

carbonate (EC, BASF)–diethyl carbonate (DEC, BASF) solution (1:1 by volume) with 1 M NaPF₆ (98%, Sigma-Aldrich) as an electrolyte, and glass fiber (Whatmann GF/F) as a separator. The cells were tested at room temperature using a Maccor 4000 battery cycler.

In Situ XRD: To probe the structural evolution of NaTi_{0.25}Fe_{0.25}Co_{0.25}Ni_{0.25}O₂ during electrochemical cycling, in situ XRD was carried out on a Bruker D8 Advance diffractometer in a reflection mode (6.5° < 2θ < 30°, Mo Kα). By using the custom-made in situ cell with a beryllium-Kapton window, the cathode was cycled at 10 mA g⁻¹ on a Solartron 1287 potentiostat, and XRD patterns were collected every 20 min, equivalent to a resolution of ≈1.4% Na per formula unit.

Transmission Electron Microscopy (TEM): TEM samples were obtained at three different states of charge (pristine and charged at 3.3 and 4.2 V) for NaTi_{0.25}Fe_{0.25}Co_{0.25}Ni_{0.25}O₂ and prepared by a drop casting method on a carbon grid. HR-STEM images were acquired by aberration corrected TEM, JEM-ARM200CF in the Condensed Matter Physics Department at Brookhaven National Laboratory and TEAM0.5 in the National Center for Electron Microscope at Lawrence Berkeley National Laboratory, operated at 200 kV at a convergence angle of ≈30 mrad using an annular dark-field imaging detector.

Computation: Density functional theory (DFT) calculations were performed with the projector augmented-wave approach, as implemented in a Vienna ab initio simulation package (VASP).^[33] The generalized gradient approximation (GGA) with the PBE functional was used for the exchange–correlation with a Hubbard *U* correction. *U* = 4.3 eV for Fe and 6.0 eV for Ni was used.^[34,35,40] The plane-wave energy cutoff was 520 eV and reciprocal space was sampled with 25 *k*-points per A⁻¹. All structures were converged to 10⁻⁶ eV in total energy and 0.02 eV A⁻¹ in forces. GGA+*U* energies were used to construct the convex energy hull. The SCAN functional (no *U* correction) was used to calculate the structural parameters of the ground state structures.^[36,47,48] A plane-wave cutoff of 520 eV, total energy convergence of 10⁻⁶ eV, and convergence of 0.02 eV A⁻¹ on forces were used in SCAN calculations.

Supercells of O3, P3, and OP2 stacking were created starting from a two-formula unit cell of Na₂FeNiO₄. The TM ordering in the unit cells of Na_{1-x}Fe_{0.5}Ni_{0.5}O₂ was kept fixed while the Na-vacancy orderings for three compositions (*x* = 0.25, 0.50, and 0.75) were enumerated across different supercell shapes (sizes): 1 × 3 × 1 (3), 2 × 2 × 1 (4), 2 × 3 × 1 (6), 1 × 1 × 6 (6), 2 × 4 × 1 (8), 3 × 3 × 1 (9), 2 × 2 × 3 (12), 1 × 4 × 4 (16), 4 × 4 × 1 (16), 2 × 4 × 2 (16), 3 × 3 × 2 (18), and 3 × 6 × 1 (18). For each supercell shape and Na content, the lowest 10 Na-vacancy orderings ranked by Ewald energy were selected as calculated in the pymatgen library^[49] and their total energy was calculated in DFT. Phase stability as a function of sodiation level was determined by calculating the convex energy hull with respect to the fully desodiated O1-Fe_{0.5}Ni_{0.5}O₂ structure and the fully sodiated O3-NaFe_{0.5}Ni_{0.5}O₂ structure.

Regardless of the stacking in the initial structure used as input for the DFT calculation, the relaxed structures based on the local NaO₆ environments were labeled using the simple chemical environment strategy in a LightStructureEnvironments pymatgen package.^[49] This algorithm identifies whether a NaO₆ local environment is prismatic or octahedral. If the structure contains only octahedral environments for Na, it is labeled O3; if it only contains prismatic environments, it is labeled P3; if there is an alternating mixture of octahedral and prismatic environments, the structure is labeled OP2. In total, there are 562 relaxed structures (181 P3 structures, 252 O3 structures, and 129 OP2 structures).

To investigate details of the subtle structural changes imposed by Jahn–Teller active Fe⁴⁺ on the NaO₆ environment, two different-sized supercells were created for each O3, P3, and OP2 stacking sequence: small (O3-Na₃₆TM₁₄₄O₂₈₈ with 9 Na layers, P3-Na₃₆TM₁₄₄O₂₈₈ with 9 Na layers, and OP2-Na₅₀TM₂₀₀O₄₀₀ with 8 Na layers) and large (O3-Na₁₈₀TM₇₂₀O₁₄₄₀ with 45 Na layers, P3-Na₁₈₀TM₇₂₀O₁₄₄₀ with 45 Na layers, and OP2-Na₂₅₀TM₁₀₀₀O₂₀₀₀ with 40 Na layers). In both the cases, 200 structures were randomly generated, oxidation states were assigned to be Na⁺, Fe⁴⁺, TM^{3,67+}, and O²⁻, and they were ranked by Ewald energy using the pymatgen algorithms.^[49] The lowest energy 100 structures were used for the simulation that is described in the Discussion section.

Supporting Information

Supporting Information is available from the Wiley Online Library or from the author.

Acknowledgements

J.C.K., D.-H.K., and J.H.Y. contributed equally to this work. This research was supported by the Samsung Advanced Institute of Technology. Work at the Molecular Foundry was supported by the Office of Science, Office of Basic Energy Sciences of the U.S. Department of Energy (DOE) under Contract No. DE-AC02-05CH11231. Work at Brookhaven National Laboratory was supported by the DOE Office of Science, Office of Basic Energy Sciences, Division of Materials Science and Engineering under Contract No. DE-SC0012704. Use of the Advanced Photon Source at Argonne National Laboratory was supported by the DOE Office of Science, Office of Basic Energy Sciences under Contract No. DE-AC02-06CH11357. This research used resources at the Spallation Neutron Source, a DOE Office of Science user facility operated by the Oak Ridge National Laboratory. The computational part of this work used computational resources sponsored by the DOE Office of Energy Efficiency and Renewable Energy and located at the National Renewable Energy Laboratory; the National Science Foundation's Extreme Science and Engineering Development Environment (XSEDE) supercomputer Stampede2 through allocation TG-DMR970008S; and the DOE, Office of Science, Office of Basic Energy Sciences, Materials Sciences and Engineering Division under Contract No. DE-AC02-05CH11231 (Materials Project program KC23MP). J.C.K. is grateful for support from the PSEG Foundation to advance energy innovation at Stevens Institute of Technology. J.H.Y. acknowledges support from the Department of Defense through the National Defense Science and Engineering Graduate Fellowship Program.

Conflict of Interest

The authors declare no conflict of interest.

Keywords

energy storage, layered structure, Na-ion batteries, O3 structure, OP2 structure

Received: April 1, 2020

Revised: June 1, 2020

Published online: June 30, 2020

- [1] H. Kim, H. Kim, Z. Ding, M. H. Lee, K. Lim, G. Yoon, K. Kang, *Adv. Energy Mater.* **2016**, *6*, 1600943.
- [2] N. Yabuuchi, K. Kubota, M. Dahbi, S. Komaba, *Chem. Rev.* **2014**, *114*, 11636.
- [3] C. Delmas, C. Fouassier, P. Hagenmuller, *Physica B+C* **1980**, *99*, 81.
- [4] S. P. Ong, V. L. Chevrier, G. Hautier, A. Jain, C. Moore, S. Kim, X. Ma, G. Ceder, *Energy Environ. Sci.* **2011**, *4*, 3680.
- [5] J. Reed, G. Ceder, *Electrochem. Solid-State Lett.* **2002**, *5*, 145.
- [6] J. Reed, G. Ceder, *Chem. Rev.* **2004**, *104*, 4513.
- [7] S. W. Kim, D. H. Seo, X. Ma, G. Ceder, K. Kang, *Adv. Energy Mater.* **2012**, *2*, 710.
- [8] H. Yao, P. Wang, Y. Wang, X. Yu, Y. Yin, Y. Guo, *Adv. Energy Mater.* **2017**, *7*, 1700189.
- [9] C. Zhao, F. Ding, Y. Lu, L. Chen, Y. S. Hu, *Angew. Chem., Int. Ed.* **2020**, *59*, 264.
- [10] M. Jeong, H. Lee, J. Yoon, W.-S. Yoon, *J. Power Sources* **2019**, *439*, 227064.
- [11] E. Talaie, V. Duffort, H. L. Smith, B. Fultz, L. F. Nazar, *Energy Environ. Sci.* **2015**, *8*, 2512.
- [12] N. Yabuuchi, M. Kajiyama, J. Iwatate, H. Nishikawa, S. Hitomi, R. Okuyama, R. Usui, Y. Yamada, S. Komaba, *Nat. Mater.* **2012**, *11*, 512.
- [13] D. D. Yuan, Y. X. Wang, Y. L. Cao, X. P. Ai, H. X. Yang, *ACS Appl. Mater. Interfaces* **2015**, *7*, 8585.
- [14] R. Berthelot, M. Pollet, D. Carlier, C. Delmas, *Inorg. Chem.* **2011**, *50*, 2420.
- [15] J. W. Somerville, A. Sobkowiak, N. Tapia-Ruiz, J. Billaud, J. G. Lozano, R. A. House, L. C. Gallington, T. Ericsson, L. Häggström, M. R. Roberts, U. Maitra, P. G. Bruce, *Energy Environ. Sci.* **2019**, *12*, 2223.
- [16] P. Vassilaras, S. T. Dacek, H. Kim, T. T. Fister, S. Kim, G. Ceder, J. C. Kim, *J. Electrochem. Soc.* **2017**, *164*, A3484.
- [17] J. L. Yue, Y. N. Zhou, X. Yu, S. M. Bak, X. Q. Yang, Z. W. Fu, *J. Mater. Chem. A* **2015**, *3*, 23261.
- [18] V. F. Sears, *Neutron News* **1992**, *3*, 26.
- [19] C. Ma, J. Alvarado, J. Xu, R. J. Clément, M. Kodur, W. Tong, C. P. Grey, Y. S. Meng, *J. Am. Chem. Soc.* **2017**, *139*, 4835.
- [20] S. J. Pennycook, *Scanning Transmission Electron Microscopy*, Springer Nature, New York **2011**.
- [21] E. J. Kirkland, *Advanced Computing in Electron Microscopy*, Springer Nature, New York **2010**.
- [22] S. J. Pennycook, P. D. Nellist, *Scanning Transmission Electron Microscopy*, Springer Nature, New York **2011**.
- [23] S. Guo, Y. Sun, J. Yi, K. Zhu, P. Liu, Y. Zhu, G. Zhu, M. Chen, M. Ishida, H. Zhou, *NPG Asia Mater.* **2016**, *8*, e266.
- [24] X. Lu, L. Gu, Y. S. Hu, H. C. Chiu, H. Li, G. P. Demopoulos, L. Chen, *J. Am. Chem. Soc.* **2015**, *137*, 1581.
- [25] M. Sathiyaa, J. Thomas, D. Batuk, V. Pimenta, R. Gopalan, J. M. Tarascon, *Chem. Mater.* **2017**, *29*, 5948.
- [26] P. F. Wang, H. R. Yao, X. Y. Liu, Y. X. Yin, J. N. Zhang, Y. Wen, X. Yu, L. Gu, Y. G. Guo, *Sci. Adv.* **2018**, *4*, eaar6018.
- [27] H. Yu, Y. Ren, D. Xiao, S. Guo, Y. Zhu, Y. Qian, L. Gu, H. Zhou, *Angew. Chem., Int. Ed.* **2014**, *53*, 8963.
- [28] H. R. Yao, P. F. Wang, Y. Gong, J. Zhang, X. Yu, L. Gu, C. Ouyang, Y. X. Yin, E. Hu, X. Q. Yang, E. Stavitski, Y. G. Guo, L. J. Wan, *J. Am. Chem. Soc.* **2017**, *139*, 8440.
- [29] X. Li, Y. Wang, D. Wu, L. Liu, S. H. Bo, G. Ceder, *Chem. Mater.* **2016**, *28*, 6575.
- [30] M. Guilmard, C. Pouillier, L. Croguennec, C. Delmas, *Solid State Ionics* **2003**, *160*, 39.
- [31] G. X. Wang, J. Horvat, D. H. Bradhurst, H. K. Liu, S. X. Dou, *J. Power Sources* **2000**, *85*, 279.
- [32] S. Muhammad, H. Kim, Y. Kim, D. Kim, J. H. Song, J. Yoon, J.-H. Park, S.-J. Ahn, S.-H. Kang, M. M. Thackeray, W.-S. Yoon, *Nano Energy* **2016**, *21*, 172.
- [33] A. Van Der Ven, J. Bhattacharya, A. A. Belak, *Acc. Chem. Res.* **2013**, *46*, 1216.
- [34] M. Aydinol, A. Kohan, G. Ceder, K. Cho, J. Joannopoulos, *Phys. Rev. B: Condens. Matter Mater. Phys.* **1997**, *56*, 1354.
- [35] Y. Hinuma, H. Hayashi, Y. Kumagai, I. Tanaka, F. Oba, *Phys. Rev. B* **2017**, *96*, 094102.
- [36] J. H. Yang, D. A. Kitchaev, G. Ceder, *Phys. Rev. B* **2019**, *100*, 035132.
- [37] J. L. Kaufman, A. Van Der Ven, *Phys. Rev. Mater.* **2019**, *3*, 015402.
- [38] X. Li, D. Wu, Y. N. Zhou, L. Liu, X. Q. Yang, G. Ceder, *Electrochem. Commun.* **2014**, *49*, 51.
- [39] X. Chen, S. Hwang, R. Chisnell, Y. Wang, F. Wu, S. Kim, J. W. Lynn, D. Su, X. Li, *Adv. Funct. Mater.* **2018**, *28*, 1803896.
- [40] P. Vassilaras, D. H. Kwon, S. T. Dacek, T. Shi, D. H. Seo, G. Ceder, J. C. Kim, *J. Mater. Chem. A* **2017**, *5*, 4596.

- [41] S. Maletti, A. Sarapulova, A. Schökel, D. Mikhailova, *ACS Appl. Mater. Interfaces* **2019**, *11*, 33923.
- [42] C. A. Marianetti, D. Morgan, G. Ceder, *Phys. Rev. B: Condens. Matter Mater. Phys.* **2001**, *63*, 224304.
- [43] R. J. Clément, Z. Lun, G. Ceder, *Energy Environ. Sci.* **2020**, *13*, 345.
- [44] A. Urban, A. Abdellahi, S. Dacek, N. Artrith, G. Ceder, *Phys. Rev. Lett.* **2017**, *119*, 176402.
- [45] Y. Mo, S. P. Ong, G. Ceder, *Chem. Mater.* **2014**, *26*, 5208.
- [46] C. L. Farrow, P. Juhas, J. W. Liu, D. Bryndin, E. S. Boin, J. Bloch, T. Proffen, S. J. L. Billinge, *J. Phys.: Condens. Matter* **2007**, *19*, 335219.
- [47] C. Shahi, J. Sun, J. P. Perdew, *Phys. Rev. B* **2018**, *97*, 094111.
- [48] D. A. Kitchaev, H. Peng, Y. Liu, J. Sun, J. P. Perdew, G. Ceder, *Phys. Rev. B* **2016**, *93*, 045132.
- [49] S. P. Ong, W. D. Richards, A. Jain, G. Hautier, M. Kocher, S. Cholia, D. Gunter, V. L. Chevrier, K. A. Persson, G. Ceder, *Comput. Mater. Sci.* **2013**, *68*, 314.